Surfaces and Interfaces 80 (2026) 108306

Contents lists available at ScienceDirect

Surfaces and Interfaces

journal homepage: www.sciencedirect.com/journal/surfaces-and-interfaces

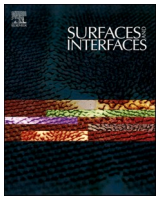

Catalytic interplay and oxygen vacancy mediation on pristine and silver doped bismuth vanadate thin films for potential ammonia detection at room temperature

Santhosh Nallakumar [a], Logu Thirumalaisamy [b], Kalainathan Sivaperuman [c], Thangavel Ravikumar [a,c], Anju Thomas [a,c], Vijaya B [a], Anand Sekar [a,d], Uma Mageshwari P [b], Manohar Darla [a], Ravi Shanker Babu [a], Usha Rani Muthurakku [a,*]

[a] Department of Physics, School of Advanced Sciences, VIT, Vellore, 632014, India
[b] Department of Physics, G.T.N Arts College (Affiliated to Madurai Kamaraj University), Dindigul, India
[c] Centre for Nanotechnology Research, VIT, Vellore, 632014, India
[d] Department of Science and Humanities, Dhanalakshmi Srinivasan College of Engineering, Coimbatore - 641105, India

ARTICLE INFO

Keywords:
Chemi-resistive gas sensor
Oxygen vacancy mediation
Doping strategy
Room temperature operation
Chemical spray pyrolysis

ABSTRACT

Revolutionized modern industries have evolved to develop tremendously potential chemi-resistive gas sensors to safeguard human health, prevent food spoilage, and improve air quality. Binary metal oxide semiconductors hold significant promise as a sensing layer in chemi-resistive gas sensors but fall short in terms of real-time flexibility, including cross-selectivity, lower operating temperature, and limit of detection. To overcome these hindrances, ternary metal oxide spinel as sensing layers have garnered significant attention due to their superior physico-chemical properties, dual cationic nature, and different valence states, etc. This work presents the deposition of pristine and silver-doped bismuth vanadate thin films using the facile chemical spray pyrolysis method. As deposited thin films were scrutinized through powder X-ray diffraction, UV–Vis spectroscopy, Raman spectroscopy, atomic force microscopy, morphological analysis, and finally their gas sensing performances were evaluated. A higher dislocated network (9.1×10^{-4}), narrowed bandgap (2.71 eV), increased surface roughness (1127 nm), enhanced oxygen vacancies (32.20 %), and smaller crystallite size (32.99 nm) facilitated enhanced gas molecule diffusion on the 5 wt.% Ag-doped $BiVO_4$ (BVA5's) film. Among various volatile organic compounds, ammonia (NH_3) is molecularly smaller in size, the presence of lone pairs of electrons in nitrogen atoms, and the catalytic effect through silver doping contribute to a high sensor response ($S = I_{gas}/I_{air} = 159$ @ 1 ppm) at room temperature (~30 °C and RH = ~52 %), demonstrating its potential for ammonia gas sensing devices.

1. Introduction

Foodborne illness affects human health, causing over 6 million cases and 400,000 deaths annually [1]. Consumers are also increasingly concerned about food quality, as consuming deteriorated food can cause numerous health problems due to the presence of viruses, toxins, parasites, and bacteria. Protein-rich foods like milk, seafood, and meat are particularly susceptible to spoilage due to the rapid growth of pathogens and microorganisms [2]. Proteolytic degradation of proteins leads to the release of ammonia and biogenic amines. Sensitive and accurate detection of these compounds provides a valuable tool for the food industry to ensure product safety and quality. Similarly, ammonia (NH_3) has several applications in refrigeration, fertilizer production, explosives manufacturing, textile processing, and polymer synthesis. However, its high toxicity poses a risk of irritation to the skin, eyes, and respiratory system upon contact or inhalation. To address all these potential health risks posed by ammonia, it is crucial to monitor and control ammonia levels in our environment [3].

Semiconductor-based metal oxide thin films are the preferred choice for chemi-resistive gas sensors [4]. Their tunable electronic properties, simple working mechanisms, and stability in harsh environments make them strong candidates in gas sensing applications [5]. Binary metal oxide based chemi-resistive gas sensors are often designed with inbuilt micro-heaters to enhance their sensing performance. However, elevated

* Corresponding author.
E-mail address: usharani.m@vit.ac.in (U.R. Muthurakku).

https://doi.org/10.1016/j.surfin.2025.108306
Received 3 March 2025; Received in revised form 18 October 2025; Accepted 10 December 2025
Available online 11 December 2025

operating temperatures can lead to grain growth, which significantly contributes to baseline drift, cross-selectivity issues, and affects the long-term stability of the sensor [6]. Although the cost of micro-heaters is minimal, higher temperature operation increases power consumption. Hence, room-temperature sensing is preferred, as it helps maintain structural stability, minimize baseline drift, reduce energy consumption. Significant efforts have been made to develop metal oxide thin film sensors that can operate at room temperature. However, binary metal oxide thin films have a few shortcomings in long-term stability, cross-selectivity, higher operating temperature, etc [7]. On the other hand, ternary metal oxide shows promise in detecting hazardous gases due to their unique physiochemical attributes, dual cations with various charge states, and leading to abundant active sites [7,8]. Monoclinic $BiVO_4$ material has attracted many researchers interest due to its high catalytic nature, narrow bandgap, and impressive potential in applications such as photocatalysis, solar cell, water splitting, and gas sensors [9,10]. Literature surveys suggest that these materials hold promise for detecting various hazardous chemicals in gas sensing applications. However, their sensing performance still needs significant improvement to be effective as gas sensors with high sensitivity and selectivity.

Doping is an intentional addition of impurities into a material's crystal lattice, that can effectively modify its physicochemical properties [11]. In this present work, we employed a strategy to introduce Ag metal ions into the lattice planes of the $BiVO_4$ material. Silver (Ag) metal atoms, with their strong affinity for oxygen species, and the spillover effect, can significantly enhance surface reactivity. The chemical spray pyrolysis method was adopted to deposit both pristine and Ag-doped $BiVO_4$ thin films. The deposited films were scrutinized through structural, optical, morphological, and elemental analysis to confirm the formation of the desired material. Further, gas sensing assessments revealed that the 5 Wt.% Ag-doped $BiVO_4$ thin film exhibited an enhanced sensor response ($S = I_{gas}/I_{air} = 159$ @ 1 ppm) and good linearity at room temperature.

1.1. Experimental method and characterizations

Bismuth nitrate pentahydrate, ammonium metavanadate, and silver nitrate are the primary metal precursors for the deposition of $BiVO_4$ thin films. An appropriate stoichiometric ratio of Bi $(NO_3)_3.5H_2O$ and NH_4VO_3 metal precursors was dissolved into 15 ml of DI water and stirred for 15 min. Silver doping was achieved by following a weight percentage approach for incorporating Ag^+ ions into the $BiVO_4$ matrix. The weight ratios of Ag^+ to Bi^{3+} used were 0:100 %, 1:99 %, 3:97 %, and 5:95 %, corresponding to BVA0, BVA1, BVA3, and BVA5 films, respectively. To improve the solution transparency of the prepared precursor, the solution was reinforced by nitric acid. While deposition was taking place, certain parameters remained unchanged: spray angle, hot plate temperature, interval, spray time, and nozzle to substrate distance were 42°, 200 °C, 10 s, 2 min, and 30 cm, respectively. The XRD diffractometer determinations using D8 - Advanced Bruker instrument helps analyse the crystal structure of the material. Raman spectrometer was used to analyse the vibration bands of the desired material using Horiba XploRA™ with a 532 nm laser source. The optical properties of the deposited thin films have been acquired from the absorbance spectrum, which was assessed through Carry UV–Vis-NIR Spectrometer. The surface roughness profiles and morphology of the thin film sensor were analysed using Nanosurf Easyscan and Carl Zessis-Sigma 300, respectively. Elemental analysis of the deposited films was carried out using Energy-Dispersive X-ray Spectroscopy (EDX) integrated with a Carl Zessis-Sigma 300 system. The chemical states and oxidation states of the constituent elements were analysed using X-ray Photoelectron Spectroscopy (XPS) performed on a Thermo Fisher Nexsa instrument equipped with an Al Kα radiation source.

1.2. Sensing layer preparation and measurements

The gas sensing efficacy was performed using a custom-built setup. To establish electrical contacts on the pristine and Ag-doped $BiVO_4$ thin films, silver conductive paste and low-resistance copper wires were employed. The electrodes were fabricated with dimensions of 1.5 cm in length and 0.25 cm in width. The distance between the electrodes, which defines the active sensing region, was maintained at 1 cm. A constant bias voltage of 5 V was applied during all sensing experiments. The thin film sensor was connected to a Keithley 6517B electrometer, and the sensing measurements were carried out using a custom-built gas sensing setup. A 1-liter Borosil glass beaker was used as the test chamber, inside which the sensor was positioned. All measurements were performed at room temperature, as schematically illustrated in Fig. 1.

To ensure a stable baseline resistance, the sensor was initially exposed to clean air before each gas measurement cycle. To introduce the volatile organic compounds in the gas phase, a standard conversion formula (shown in Eq. (1)) was utilized to determine the appropriate liquid volume [12].

$$C_{(ppm)} = \frac{\delta \times V_\Gamma \times R \times T \times 10^6}{M \times P_b \times V_b} \quad (1)$$

Where, The density of the target molecule – δ, The molecular weight of the VOC – M, Net volume of DMA purged inside the chamber - Vr, Chamber volume in liters - Vb, Universal gas constant – R, Absolute temperature – T, Chamber pressure - Pb, respectively.

The calculated amount of volatile liquid was then injected into the Borosil test chamber, where it rapidly vaporized and interacted with the sensor film. This interaction led to a measurable variation in the electrical current. The sensor response (S) was determined by calculating the ratio of the current measured in the presence of the analyte gas (I_{gas}) to that measured in clean air (I_{air}). The response and recovery times were defined as the duration required for the sensor to reach 90 % of the total current change during the adsorption and desorption cycles, respectively. To evaluate the sensor's resistance to moisture interference, the sensing film was also tested under varying relative humidity conditions.

2. Result and discussion

2.1. Structural analysis

The Fig. 2(a) illustrates the diffraction patterns obtained from the spray-deposited pristine and Ag doped $BiVO_4$ thin films. The typical diffraction peaks observed at 18.91, 28.94, 30.56, 35.13, 39.96, 42.94, 46.91, 47.22, 50.26, 53.33 are close match with lattice planes of (011), (121), (040), (002), (−112), (051), (132), (042), (202), (310), which affirms the formation of standard monoclinic $BiVO_4$ structure (ICDD. No: 014–0688) [13]. To the successful integration of silver, 1–5 Wt.% of Ag was incorporated as a dopant into the lattice sites of the $BiVO_4$ thin film. As a consequence, no secondary phase formation was observed in

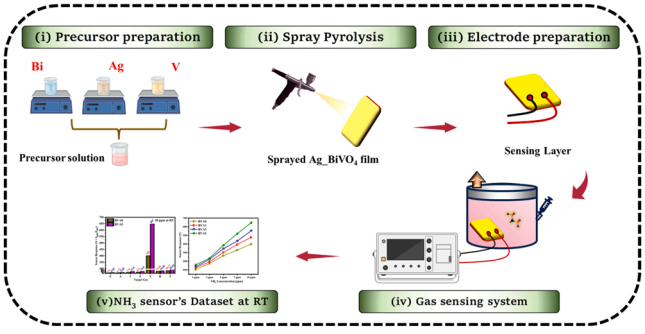

Fig. 1. Schematic illustration of precursor preparation, thin film deposition, and gas sensing measurements for pristine and Ag doped $BiVO_4$ films.

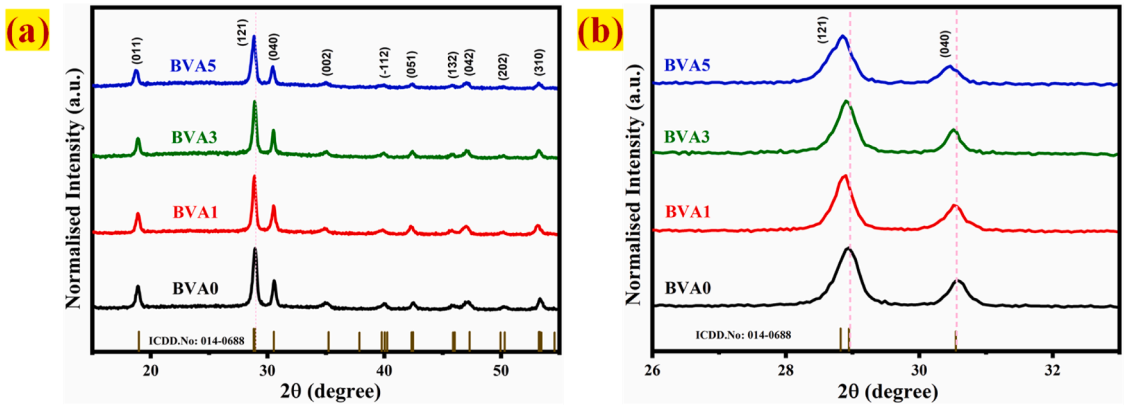

Fig. 2. (a) XRD patterns of pristine and Ag-doped $BiVO_4$ thin films; (b) enlarged section of the diffraction peaks in the 2θ range of 26–33°.

the diffracted pattern. Subsequently, a slight lower angle shift was observed in the Ag-doped $BiVO_4$ thin film's diffracted pattern (shown in Fig. 2(b)), which is due to the difference in ionic radius between Ag^{1+} (126 pm) and Bi^{3+} (103 pm). A significant shift in peak position corroborates the successful integration of Ag atoms and the formation of monoclinic $BiVO_4$ thin films. The deposited film's lattice parameters, cell volume, crystallite size, dislocation density, and microstrain were calculated and are tabulated in the Table 1. The related formulas were acquired from our previous publication [14]. The lattice constants of the monoclinic $BiVO_4$ crystal system showed excellent agreement with those of our deposited films. The introduction of dopant atoms into the $BiVO_4$ material leads to significant lattice deformations, which in turn drive the observed trend. The pristine $BiVO_4$ film exhibited a higher crystallite size and lower dislocation density. After the incorporation of Ag atoms into the monoclinic $BiVO_4$ crystal system, dislocation density increased, while crystallite size was reduced. The reduced crystallite size enhances surface area by increasing the number of particles and their surface-to-volume ratio [15,16]. Concurrently, increased dislocation density creates a rougher surface with more irregularities, also enhancing the total surface area of the material. This increased surface area facilitates the diffusion of a greater number of gas molecules, potentially enhancing the gas response.

Fig. 3 depicts four distinct vibrational modes (212.07, 331, 369.2, and 821 cm^{-1}) are correspond to monoclinic $BiVO_4$, which are aligned with earlier reports [13,17]. The prominent vibrational mode is situated at 821 cm^{-1} and is associated with symmetric V-O stretching modes [18,19]. Similarly, two weaker vibrational modes at 331 and 369.2 cm^{-1} are related to the asymmetric and symmetric vibrations of the VO_4^{3-} ion, respectively [18–20]. Subsequently, another vibrational band at 212.07 cm^{-1} can be attributed to external translation/vibrational modes [18,20]. As the concentration of Ag atoms increased, the Raman intensity decreased linearly and exhibited a gradual shift toward lower wavenumber. This reduction may be attributed to dopant-induced lattice strain and defect formation within the system [21], which is in accordance with the XRD analysis.

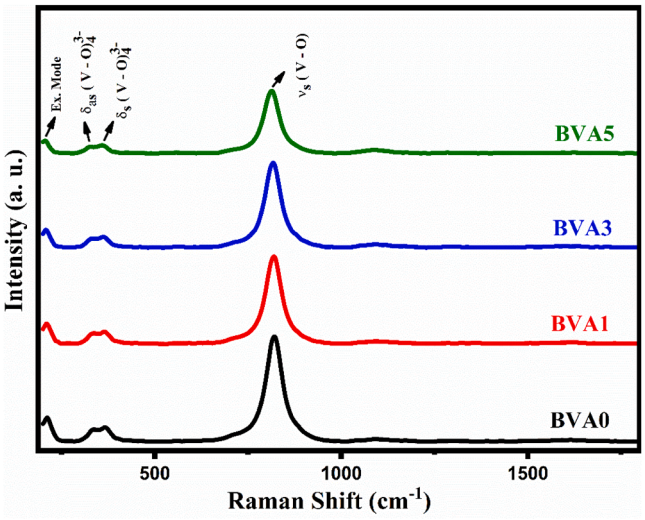

Fig. 3. Depicts the vibrational modes of pristine and Ag-doped $BiVO_4$ thin films.

2.2. Optical analysis

UV–Vis spectroscopy was employed to investigate the optical properties of the deposited thin films. As depicted in Fig. 4, the absorbance spectra of BVA0, BVA1, BVA3, and BVA5 thin films exhibit a clear trend of a decrease in absorbance with increasing Ag doping concentration. The deposited films had a rise in absorbance edge is 430, 442, 449, and 457 nm, for BVA0, BVA1, BVA3, and BVA5 films, respectively. The optical bandgap of the deposited film, which corresponds to the energy separation between the valence and conduction bands, was estimated using the Tauc method.

Eq. (2) describes the relationship between a material's absorption coefficient (α) and its optical bandgap (Eg) as follows.

$$(\alpha h\upsilon)^m = K(h\upsilon - Eg) \quad (2)$$

Table 1
Illustrates data sets from pristine and Ag-doped $BiVO_4$ thin films.

Sample	Lattice constant (Å)			Cell volume (Å^3)	Micro strain (line $^{-2}$ m^{-4}) (x 10^{-2})	Dislocation density (nm^{-2}) (x 10^{-4})	Crystallite size (nm)
	(a)	(b)	(c)				
BVA0	5.0421	11.5460	5.0889	296.26	1.7	7.5	36.33
BVA1	5.0480	11.5588	5.0895	296.94	1.8	7.9	35.43
BVA3	5.0568	11.5693	5.0905	297.81	2.1	8.7	33.89
BVA5	5.0622	11.5778	5.1058	299.24	2.4	9.1	32.99

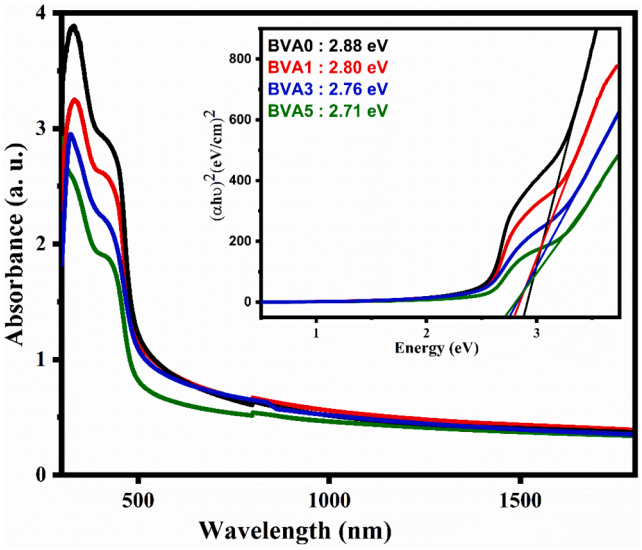

Fig. 4. Illustrates the absorbance spectrum of pristine and Ag-doped $BiVO_4$ thin films (the tauc plot from the inset image depicts the optical bandgap of the pristine and Ag-doped $BiVO_4$ thin films).

Where, Photon energy (hυ), bandgap energy (E_g), Allowed direct transition ($m = 2$) and Constant (K). The estimated bandgap energies were found to be 2.88 eV, 2.80 eV, 2.76 eV, and 2.71 eV for BVA0, BVA1, BVA3, and BVA5 films, respectively. The bandgap energy is influenced by several parameters, which includes crystallite size, carrier concentration, lattice strain, and the presence of impurities [22,23]. Among these, oxygen vacancies play a significant role in altering the electronic structure of a material by introducing localized energy levels within the bandgap. These localized states facilitate electron transitions with lower energy requirements, thereby effectively narrowing the optical bandgap [24]. In this work, the optical bandgap energy decreases from 2.88 eV (BVA0) to 2.71 eV (BVA5). This reduction is mainly attributed to the hybridization between O 2p (valence band) and V 3d (conduction band) states. Upon Ag doping into $BiVO_4$, the Ag 4d and 5 s orbitals interact with O 2p orbitals, introducing additional localized states near the valence band maximum (VBM). This interaction raises the valence band edge, resulting in a reduced bandgap energy, as the energy difference between the conduction band minimum (CBM) and the modified VBM becomes smaller [25,26]. Furthermore, Regmi et al. [27] reported a red-shifted absorption in the range of 430–457 nm upon Ag incorporation into $BiVO_4$. This phenomenon can be ascribed to the surface plasmon resonance (SPR) effect of silver nanoparticles, which originates from the collective oscillation of free conduction-band electrons excited by incident electromagnetic radiation. The localized plasmonic field enhances visible-light absorption and introduces additional electronic states near the valence band, effectively narrowing the bandgap and causing a redshift in the absorption edge.

2.3. Topographical analysis

Contact mode - Atomic Force Microscopy (AFM) was employed to investigate the surface topographical profiles of pristine and Ag-doped $BiVO_4$ thin films to understand their influence on the material's sensitivity at 50 × 50 μm (shown in Fig. 5 (a-h)) [28]. The surface roughness (Sa) and root mean square (RMS) roughness (Sq) values of chemically sprayed BVA0, BVA1, BVA3, and BVA5 thin films are 568.64 nm, 635.51 nm, 814.88 nm, 1127.8 nm and 693.37 nm, 773.72 nm, 1064.9 nm, 1525.9 nm, respectively. These observations revealed a non-uniform distribution of grains, accompanied by an increase in surface roughness with increasing Ag concentration. Surface irregularities, such as surface roughness and RMS roughness, can enhance the diffusion of target gas molecules [29]. These features increase the effective surface area available for gas interaction, potentially enhancing the gas response of the BVA5 thin film.

2.4. Morphological & elemental analysis

The morphological characteristics of chemically sprayed pristine and Ag-doped $BiVO_4$ thin films were investigated using field emission scanning electron microscopy (FE-SEM), as illustrated in Fig. 6. FE-SEM images of BVA0, BVA1, BVA3, and BVA5 thin films are presented in Fig. 6 (a, d, g, and j) and Fig. 1 (a-d) of the Supporting Information. This scrutinization revealed that spray-deposited pristine and Ag-doped $BiVO_4$ thin films exhibited well-crystallized, irregular nanograins with a uniform morphology. As the Ag composition increases, the morphology of the irregular nanograins becomes more truncated. This leads to the formation of smaller, more numerous nanograins. The average particle sizes of the deposited films with varying Ag concentrations were quantified and are presented in Fig. 6 (b, e, h, and k). The average particle sizes of the BVA0, BVA1, BVA3, and BVA5 thin films are

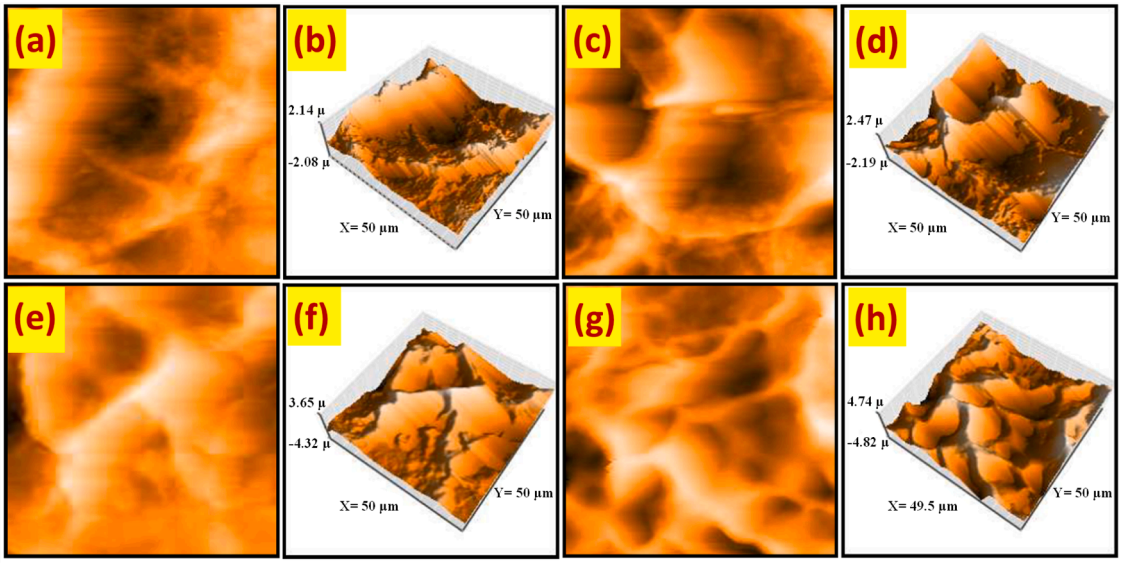

Fig. 5. Illustrates the 2D and 3D topographical profiles of BVA0 (a & B), BVA1 (c & d), BVA3 (e & f), and BVA5 (g & h) thin films, respectively.

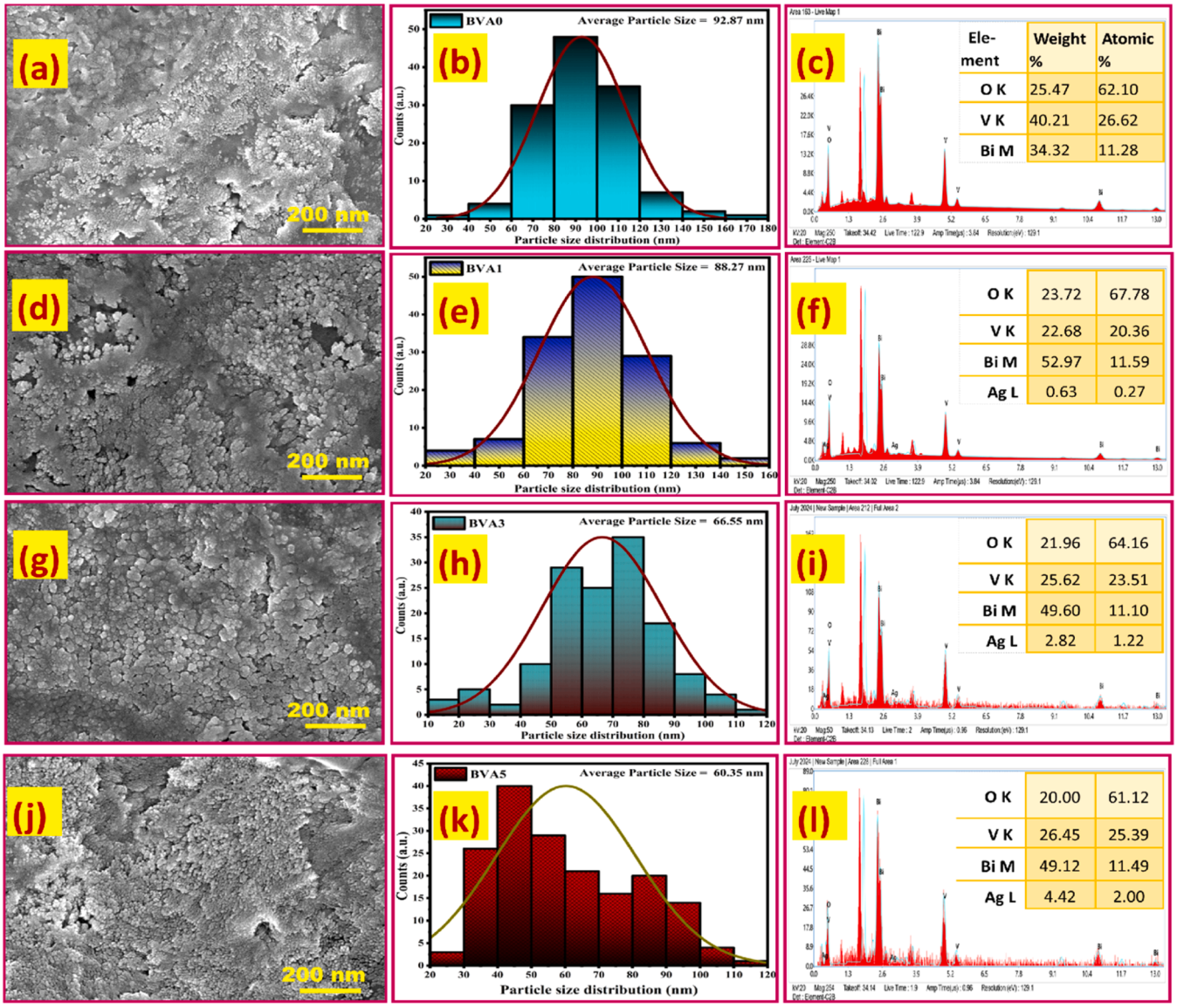

Fig. 6. (a, d, g and J) depicts the FE-SEM morphology of the deposited spray BVA0, BVA1, BVA3, and BVA5 films, (b, e, h and k) average particle size of BVA0, BVA1, BVA3, and BVA5 films from ImageJ software, and (c, f, i and l) elemental quantification of BVA0, BVA1, BVA3, and BVA5 films through EDAX, respectively.

92.87 nm, 88.27 nm, 66.55 nm, and 60.35 nm, respectively (shown in Table 2). In comparison with the other deposited films, the BVA5 thin film exhibited a smaller particle size. This suggests that the BVA5 film possesses a higher surface area, which facilitates enhanced interaction with target gas molecules.

The Energy-dispersive X-ray spectroscopy (EDX) analysis, including elemental colour mapping, was performed on BVA0, BVA1, BVA3, and BVA5 thin films to determine their elemental composition. The results are presented in Fig. 6 (c, f, i, and l) and Fig. 7 (a-p). The pristine films exhibited the presence of Bi, V, and O, consistent with monoclinic $BiVO_4$ thin film. EDX analysis revealed Ag atom weight percentages of 0.63, 2.82, and 4.43 for 1, 3, and 5 wt.% Ag doping, respectively, confirming the successful integration of Ag atoms into the monoclinic $BiVO_4$ thin film. These values are consistent with the expected experimental concentrations.

The X-ray photoelectron spectroscopy (XPS) was employed to scrutinize the surface elemental composition and the chemical states of the spray-deposited pristine and Ag-doped $BiVO_4$ thin films [30], shown in Fig. 8 (a-h). The survey spectrum (Fig. 8a) of the BVA0 and BVA5 films reveals the presence of Bi, V, O 1 s, and Ag elements. Two prominent peaks were observed at 158.81 eV and 164.10 eV (in Fig. 8b), corresponding to the Bi 4f $_{7/2}$ and Bi 4f $_{5/2}$ core levels, respectively. The resulting spin-orbit splitting energy of 5.3 eV is characteristic of the Bi^{3+} oxidation state [31].

Fig. 8d exhibits two characteristic peaks centred around 516.44 eV and 523.67 eV, which are primarily attributed to V 2p $_{3/2}$ and V 2p $_{1/2}$, respectively. The observed spin-orbit splitting energy of 7.23 eV is indicative of the V^{5+} oxidation state [32]. Fig. 8 (c and e) shows the high-resolution scans of Bismuth (Bi 4f) and Vanadium (V 2p) for

Table 2
Presents the bandgap, root mean square (RMS) roughness, surface roughness, and average particle size for pristine and Ag-doped $BiVO_4$ thin films.

Sample	Band gap (eV)	RMS roughness (Sq)	Surface roughness (Sa)	Average particle size (nm)
BVA0	2.88	693.37	568.64	92.87
BVA1	2.80	773.72	635.51	88.27
BVA3	2.76	1064.90	814.88	66.55
BVA5	2.71	1525.90	1127.80	60.35

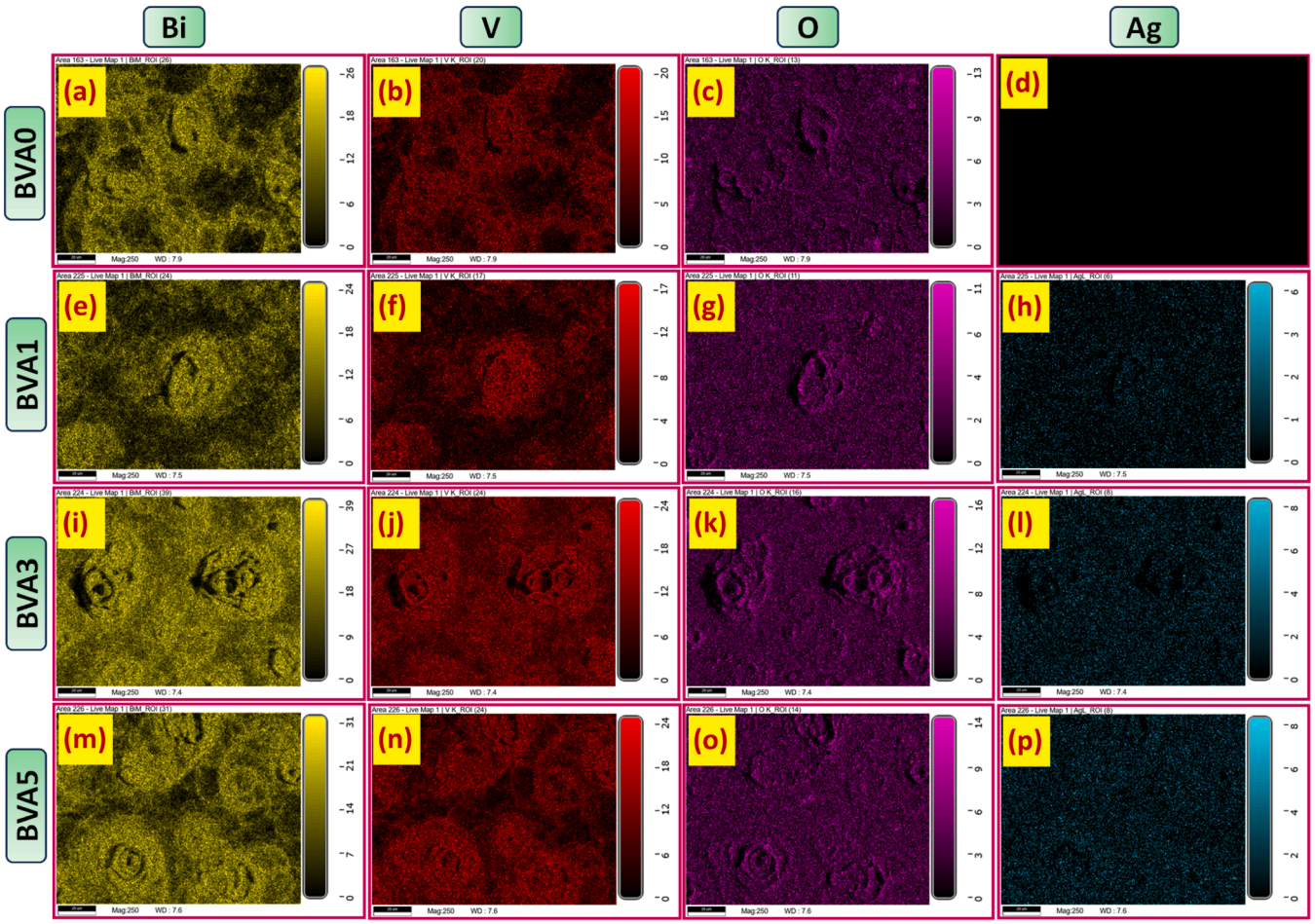

Fig. 7. (a-p) presents the FE-SEM EDAX elemental color mapping images, which disclose the uniform distribution of Bi, V, O and Ag elements in spray deposited BVA0, BVA1, BVA3, and BVA5 thin films.

BVA5's film, respectively. Peaks at 158.95 and 164.35 eV correspond to the core levels of Bi 4f 7/2 and Bi 4f 5/2, while peaks at 517.09 and 524.40 eV correspond to the core levels of V 2p 3/2 and V 2p 1/2. The corresponding orbital energy difference of 5.4 eV for Bi 4f and 7.31 eV for V 2p corroborate the oxidation states of Bi $^{3+}$ and V $^{5+,}$ respectively [31,32]. Furthermore, the observation of two extra peaks (160.10 and 165.58 eV) alongside four deconvoluted peaks in the Bi 4f spectrum (Fig. 8b) might be attributed to changes in crystal polarization due to the surface charge effect [33]. The successful integration of Ag atoms is evidenced by the presence of Ag 3d $_{5/2}$ and Ag 3d $_{3/2}$ core level peaks at 368.20 and 374.03 eV, respectively, in the Ag 3d high-resolution scan (Fig. 8f), confirming the presence of metallic silver [34]. Subsequently, Ag atom integration did not alter the orbital energy difference of Bi 4f and V 2p high-resolution scans, indicating that both BVA0 and BVA5 films exhibit the same oxidation state and crystal structure, consistent with the diffraction pattern. O 1 s spectra reveal core level oxygen contributions in BVA0 and BVA5 films (Fig. 8g and h). The peaks at 529.48 eV in BVA0 and 529.49 eV in BVA5 indicate to lattice oxygen. Similarly, peaks at 530.40 eV (BVA0) and 530.30 eV (BVA5) are attributed to defective oxygen (OD), while those at 532.68 eV (BVA0) and 532.30 eV (BVA5) are assigned to hydroxide ions [14,35]. The BVA5 film exhibited a significantly higher proportion of defective oxygen (32.20 %) than BVA0 (25.78 %). These are known to be oxygen vacancies and act as active sites for the chemisorption of oxygen species, thereby enhancing gas sensing performance [36,37]. The increased concentration of defective oxygen in the BVA5 film likely contributes to its superior sensing capabilities toward the target gas.

2.5. Gas sensing evaluation

The adsorption/desorption theory has been preconized as the primary mechanism underlying the operation of chemi-resistive gas sensors [38]. Commonly, oxygen molecules (presence in the air) are readily adsorbed on their surface and interfaces of the deposited sensing layer. Those oxygen molecules interact with electrons from sensing material, get ionized, and are converted into O^{2-} (below 420 K), O^{-} (mid 420 K - 670 K), and O_2^- (above 670 K). As a result, the number of holes in the semiconductor (at the core) increased, leading to an increase in resistance. NH_3 gas is introduced into the chamber, readily available surface adsorbed ionized species react with the target gas (shown in below the equation), as a by-product electrons were reinserted to the material.

$$\mathbf{NH_3\ (gas) \rightarrow NH_3\ (surface\ ads)} \tag{3}$$

$$\mathbf{4NH_{3\ (surface\ ads)} + O_2^-(ionized\ species\ ads) \rightarrow 2\ N_2 + 6H_2O + 3e^-} \tag{4}$$

Due to these actions, the hole concentration was reduced, resulting in a corresponding decrement in the resistance [5,38,39]. In this current work, we have deposited pristine and Ag-doped thin films to scrutinize their gas sensing efficacy at room temperature. For a potential gas sensor, a stable baseline current is imperative one. Hence, the saturated baseline current of the prepared thin film sensors was exhibited at 3.64, 3.79, 3.85, and 4.07×10^{-10} A for BVA0, BVA1, BVA3, and BVA5, respectively.

The pristine BVA0 film's gas sensing capabilities of the volatile organic compounds like ethanol ($S = I_{gas}/I_{air} = 3.0$), acetone ($S = I_{gas}/$

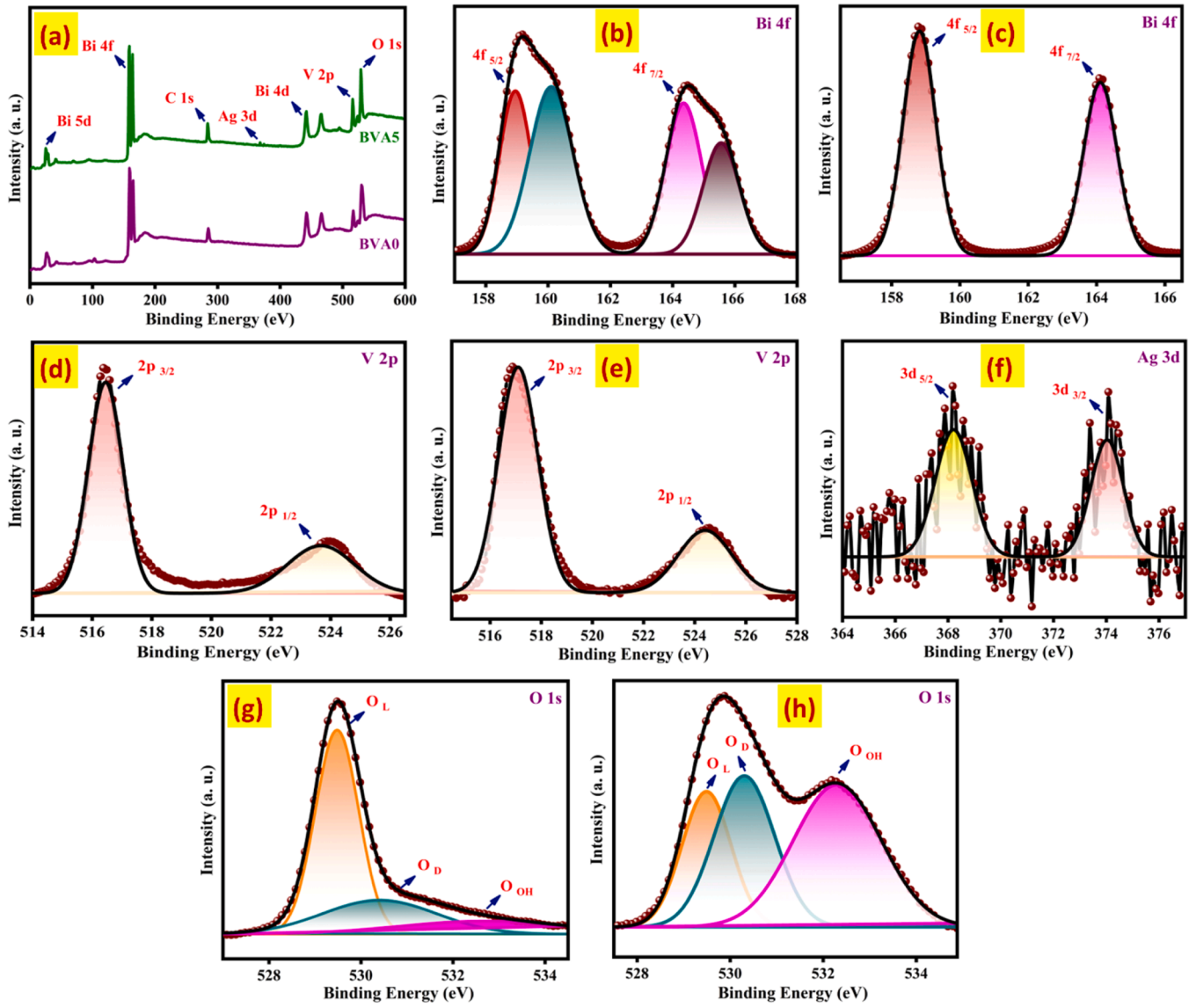

Fig. 8. XPS survey spectrum and high-resolution scans of pristine (BVA0) and 5 wt.% Ag-doped $BiVO_4$ thin films (BVA5). (a) Survey spectra of BVA0 and BVA5 film; (b, c) Bi 4f high-resolution spectra of BVA0 and BVA5 film, respectively; (d, e) V 2p high-resolution spectra of BVA0 and BVA5 film, respectively; (f) Ag 3d high-resolution spectrum; (g, h) O 1 s high-resolution spectra of BVA0 and BVA5 film, respectively.

$I_{air} = 4.13$), 2-propanol ($S = I_{gas}/I_{air} = 7.0$), formaldehyde ($S = I_{gas}/I_{air} = 9.0$), ammonia ($S = I_{gas}/I_{air} = 440$), dimethylamine ($S = I_{gas}/I_{air} = 15.3$), and trimethylamine ($S = I_{gas}/I_{air} = 20.31$) were tested for 10 ppm at room temperature (~30 °C and RH = ~52 %). Subsequently, the BVA5 thin film sensor's sensor responses are such as ethanol ($S = I_{gas}/I_{air} = 5.29$), acetone ($S = I_{gas}/I_{air} = 6.29$), 2-propanol ($S = I_{gas}/I_{air} = 13.5$), formaldehyde ($S = I_{gas}/I_{air} = 14$), ammonia ($S = I_{gas}/I_{air} = 637$), dimethylamine ($S = I_{gas}/I_{air} = 18.46$), and trimethylamine ($S = I_{gas}/I_{air} = 29.92$) were tested for 10 ppm at room temperature, respectively. Interestingly, BVA5 revealed the highest sensor response to ammonia gas than other target gases, which is shown in Fig. 9(a). The BVA5 film's highest sensor response to NH_3 gas can be attributed to the following (i) The smaller size of NH_3 molecules compared to other target gases allows for easier diffusion through the irregular nanograin morphology of the sensing material. This enhanced diffusion facilitates the interaction of ammonia molecules with the sensing material, leading to more efficient electron transfer processes and a higher sensor response [40]. (ii) Ammonia molecules readily donate electrons to the vanadium localized sites (V^{5+}) within the sensing material at room temperature. (iii) The presence of a lone pair of electrons on the ammonia molecule enhances its interaction with the sensing layer. This strong interaction contributes significantly to the improved sensor response towards ammonia vapor [41]. (iv) Compared to BVA0, BVA1, and BVA3 films, the numerous nanograins of the BVA5 film provide a larger surface area and more accessible sites for ammonia vapor adsorption, which in turn facilitates greater oxygen molecule adsorption. (v) The integration of noble Ag atoms significantly enhances the sensing response of the BVA5 film. Ag atoms exhibit high catalytic activity, which facilitates the oxidation process at the sensor surface [42]. As a consequence, an increased concentration of ionized oxygen species was generated and the excess electrons were released during the catalytic reaction. Furthermore, Ag atoms act as catalysts to form O_2^- ions during the adsorption and desorption of oxygen (O_2), increasing the overall surface coverage of adsorbed oxygen species and promoting their conversion to readily reactive forms. The abovementioned reasons are the primary factors contributing to the enhanced sensing response of the BAV5 thin film sensor to ammonia at room temperature. The dynamic sensor response of the BVA0, BVA1, BVA3, and BVA5 films were tested to NH_3 vapor at different concentrations of 1–10 ppm at room temperature is shown in Fig. 9(b) and Fig. 2- 4 in Supplementary information, respectively. The

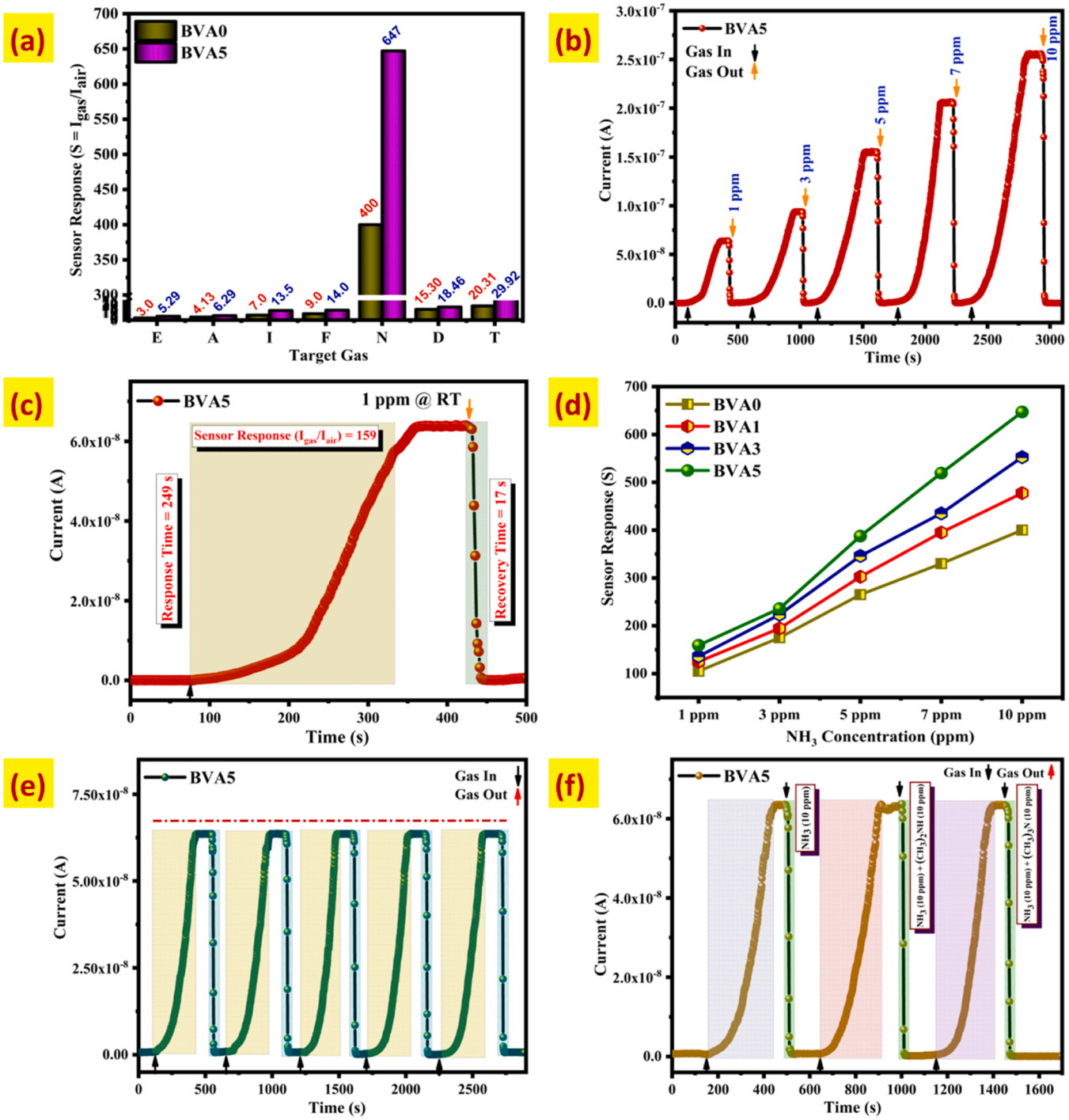

Fig. 9. Depicts the gas sensing performance toward NH_3 at room temperature (all gases tested at 10 ppm concentration): (a) selectivity of pristine $BiVO_4$ (BVA0) and 5 wt% Ag-doped $BiVO_4$ (BVA5) thin films toward ethanol (E), acetone (A), 2-propanol (I), formaldehyde (F), ammonia (N), dimethylamine (D), and triethylamine (T); (b) transient response curve of the BVA5 thin film; (c) response and recovery times of the BVA5 thin film; (d) sensor response of pristine and Ag-doped films as a function of NH_3 concentration; (e) repeatability of the BVA5 thin film; and (f) cross-selectivity of the BVA5 thin film under 1 ppm of interference from various volatile organic compounds.

sensor response of the BVA0 film ($S = I_{gas}/I_{air} = 440$) was significantly higher than those of BVA1 ($S = I_{gas}/I_{air} = 504$), BVA3 ($S = I_{gas}/I_{air} = 574$), and BVA5 ($S = I_{gas}/I_{air} = 637$), with enhancements of 1.14, 1.30, and 1.44 times to 10 ppm, respectively. Hence, as the ammonia concentration increases, the sensor exhibits a good linearity in sensor response, confirming its suitability for ammonia detection (Fig. 9(d). The BVA5 thin film has a higher dislocated network, larger surface roughness, and reduced average particle size corroborates sensing layer contains a higher number of active sites, which leads to achieve higher sensor response than other sensing layers. An ideal gas sensor's key parameters are known as response time and recovery time, which are illustrated in Fig. 9(c). The obtained response time and recovery times for both BVA0 and BVA5 films are 235 s, 249 s and 11 s, 17 s, respectively, corresponding to the gas concentration of 1 ppm at room temperature. For a commercial gas sensor, imperative features are excellent sensor response, prolonged stability, and a highly reversible one. The

Fig. 9(e) illustrates the reproducibility plots of the BVA5 thin film sensor towards NH_3 at 1 ppm (to room temperature) for continuous five cycles to test their potential. Hence, the observed sensor response of the BVA5 films is 159, 157, 158, 159, and 156, respectively. The obtained values remain almost the same, which confirms that the BVA5 thin film sensor is highly repeatable. The prolonged stability of the gas sensor is a crucial parameter for real-time applicability; So that, it's mandatory to mention that after 70th day BVA5 thin film sensor displayed the sensor response of 156 for 1 ppm to NH_3 at room temperature (shown in Fig. 10a). There is no considerable reduction in the sensor response, which are the solid evidences for a commercial gas sensor.

Fig. 9(f) illustrates the cross-selectivity of various target gases towards ammonia vapor. This plot depicts the BVA5 thin film sensor's overall efficacy towards NH_3 target gas alongside mixtures of other gases (DMA and TMA vapor) as interference. The BVA5 film exhibited a sensor response of about 158.5 for a 1 ppm concentration of NH_3 vapor alone. When interfered with target gases such as DMA + NH_3 and TMA + NH_3 at 1 ppm, the sensor responses were shown to be ($S = I_{gas}/I_{air} = 156$) and ($S = I_{gas}/I_{air} = 159$), respectively. These results demonstrate that the observed sensor response was relatively stable, indicating that the BVA5 film exhibits high selectivity towards NH_3 at room temperature. The ability of a chemi-resistive gas sensor to tolerate humidity is crucial for its practical applications.

To evaluate the moisture-resisting traits of the BVA5 thin film sensor by varying humidity levels, saturated salt solutions were used to achieve 11 % (LiCl), 32 % ($MgCl_2$), 52 % ($Mg(NO_3)_2$), and 75 % (NaCl) relative humidity (RH), respectively. The sensing measurements were performed at RT under a constant 1 ppm concentration of ammonia (NH_3) vapor (Fig. 10b). Under ambient conditions, oxygen molecules are chemisorbed onto the sensor surface, stabilizing the baseline current at approximately 4.09×10^{-10} A. Exposure to humid environments causes hydroxylated water molecules to replace chemisorbed oxygen species on the sensor surface, resulting in a slight increase in baseline current.

This rise is primarily attributed to the formation of a proton-conducting layer induced by water adsorption, which enhances surface conductivity of a BVA5 sensor film [14,43]. Even at elevated humidity levels, the sensor's performance remained largely unaffected, with only a minor increase in response and recovery times observed at room temperature (Fig. 10d). Notably, across all tested humidity levels (11–75 % RH), the sensor maintained a consistent response with fluctuations limited to <3 % (Fig. 10c). At lower humidity levels (e.g., 11 % RH), the sensor exhibited an enhanced response, which can be attributed to the presence of water vapor acting as a reactive medium that facilitates catalytic interactions, thereby boosting the sensing signal. However, as the humidity increases, a gradual decline in sensor response is observed. This reduction is likely due to the competitive adsorption between water molecules and NH_3 vapor, which limits the availability of active sites for NH_3 interaction [44]. Additionally, under higher humidity conditions, the response time becomes longer, primarily because NH_3 molecules require more time to access and interact with the fewer available active sites on the sensor surface [45]. These factors are likely responsible for the observed variations in the performance of BVA5 film sensing layer at room temperature.

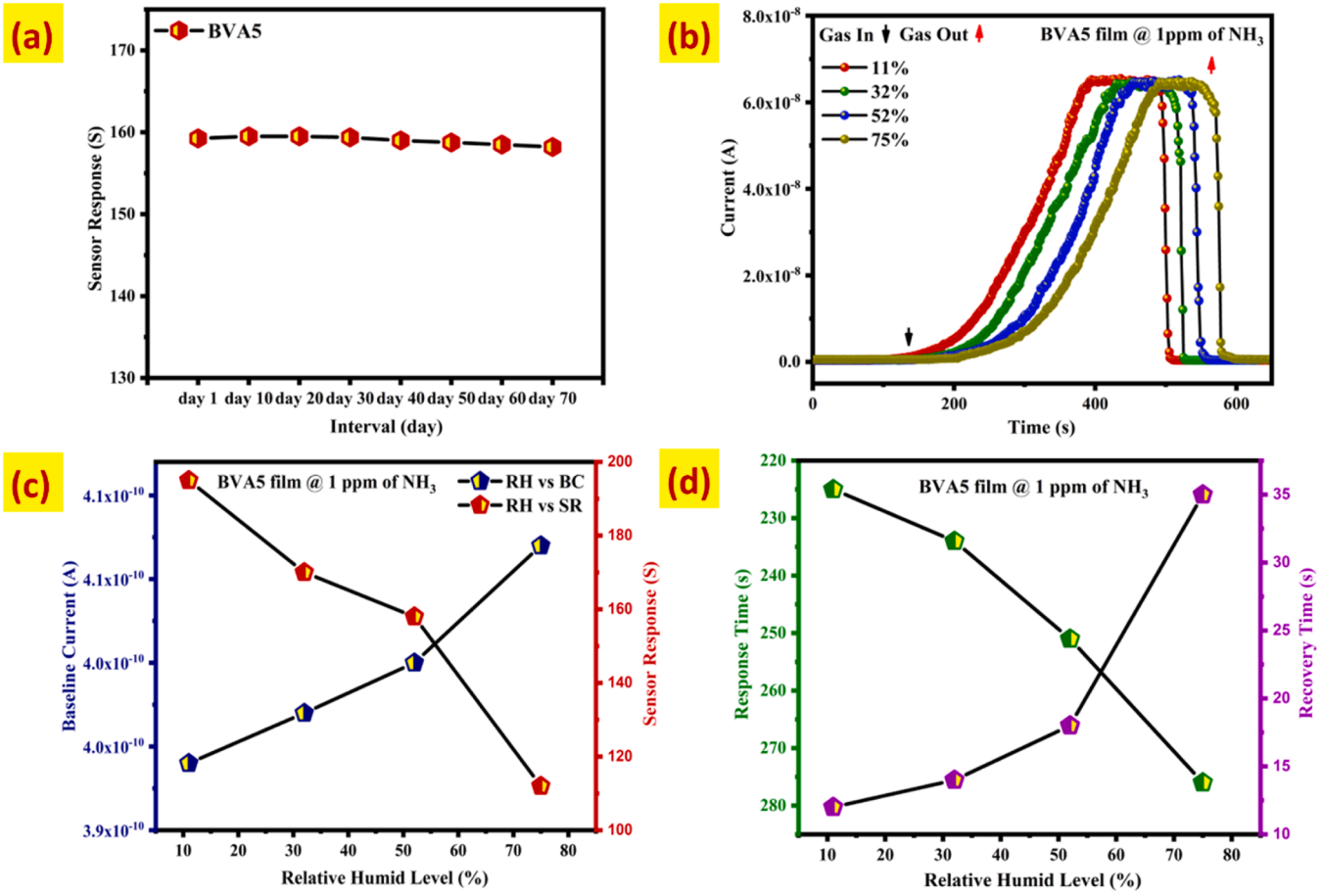

Fig. 10. (a) Shows the stability of the 5 wt.% Ag doped BiVO4 thin films (BVA5), (b) depicts the moisture resistance characteristics of the BVA5 film; (c) variation in baseline current and corresponding sensor response under different relative humidity (RH) levels; (d) influence of RH on response and recovery times of the BVA5 film.

2.6. NH_3 mechanistic discussion

The sensing mechanism of semiconducting metal oxide based chemiresistive gas sensors is primarily governed by the grain boundary model, which has been extensively studied over the years [5,39]. The schematic representation of the gas sensing mechanism is illustrated in Fig. 11a. In the air environment, oxygen molecules adsorb onto the surface of the BVA5 thin film sensor and extract electrons from its conduction band, forming chemisorbed oxygen species (O_2^-, O^-, O^{2-}) [46,47]. This process thickens the electron depletion layer (Fig. 11b), leading to an increase in the sensor's resistance. Upon exposure to ammonia, the NH_3 molecules interact with negatively charged chemisorbed oxygen species (i.e., O_2^-) on the BVA5 thin film surface, leading to the release of electrons back into the conduction band. This electron injection reduces the width of the electron depletion layer and subsequently decreases the sensor's resistance. As illustrated in Fig. 11a, the sensing mechanism at room temperature primarily involves the reaction of NH_3 with surface adsorbed oxygen ions, generating N_2 rather than NO_2, which aligns with Eqs. (3 and 4). Notably, literature reports indicate that the oxidation of NH_3 into NO or NO_2 is negligible at room temperature and becomes significant only at higher temperatures [3,35,48,49].

The incorporation of Ag atoms into the $BiVO_4$ lattice (BVA5) enhances gas sensing performance through catalytic and electronic effects. Ag facilitates faster surface redox reactions by accelerating electron transfer and promoting the formation of reactive oxygen species. It also improves the adsorption and activation of oxygen molecules, enabling efficient O_2^- generation during gas interactions [34]. These effects collectively increase active surface sites and boost gas conversion efficiency, leading to the improved sensor response and selectivity of BVA5 toward NH_3 at room temperature. In Ag doped $BiVO_4$ (BVA5) thin films, a similar sensing mechanism takes place, as described by Eq. (3). When NH_3 vapors are introduced into the sensing chamber, the ammonia molecules interact with the pre-adsorbed oxygen species (such as O_2^-) on the BVA5 surface. This reaction results in the formation of H_2O and N_2, simultaneously releasing free electrons back into the conduction band [35,48]. As a consequence, the space charge region becomes narrower (Fig. 11c), leading to an increase in the electrical conductivity of the BVA5 sensing layer. Among the fabricated sensing layers, the BVA5 sensor exhibited the most effective ammonia gas sensing performance, which can be attributed to its distinctive irregular nanograin morphology with an average particle size of approximately 60.35 nm. This architecture offers an extended percolation network that promotes greater adsorption of ionized oxygen species and facilitates the diffusion of NH_3 molecules toward the active sites for redox reactions.

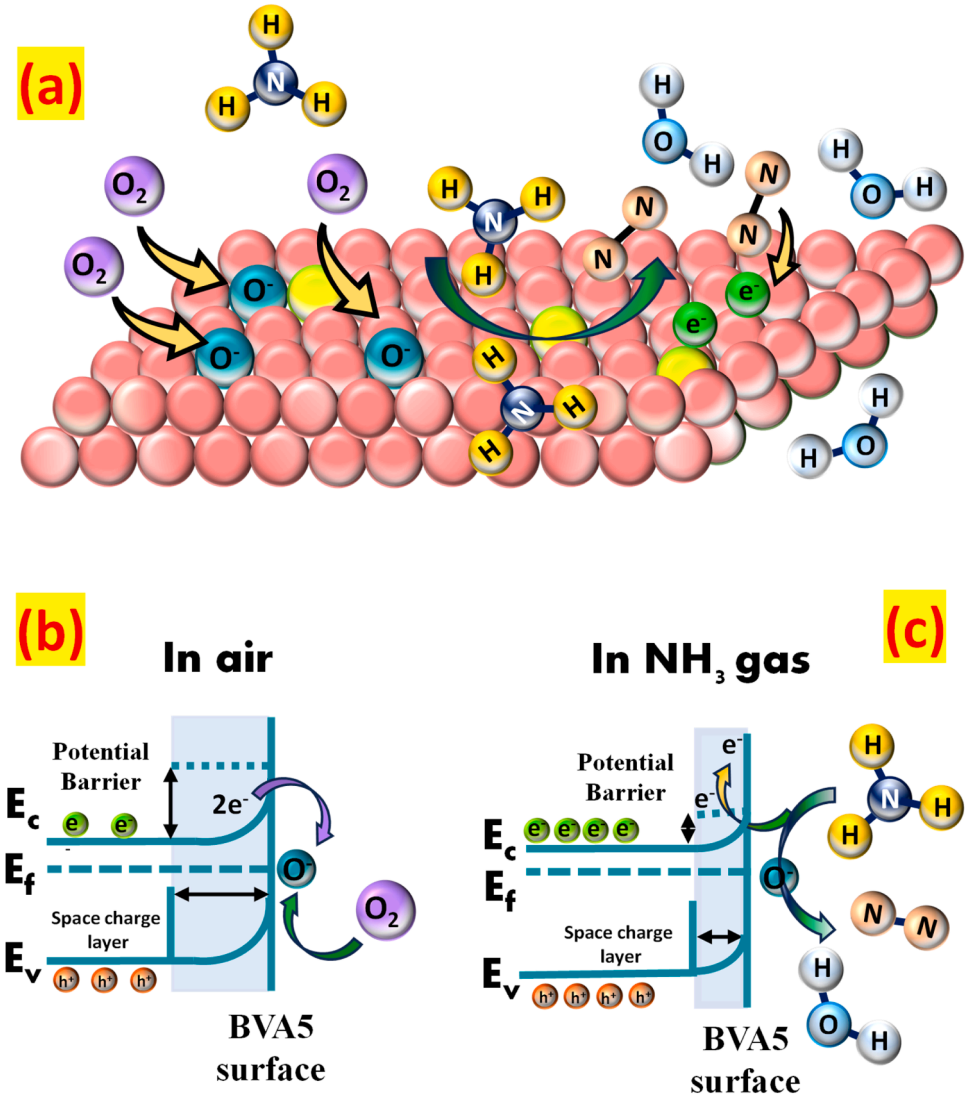

Fig. 11. (a) Schematic representation of the NH_3 sensing mechanism in the BVA5 film. (b) and (c) Illustrate the modulation of the space charge layer before and after exposure to NH_3, respectively.

Moreover, the presence of well-defined and abundant grain boundaries in the BVA5 film enhances electron transport during gas interactions, resulting in an elevated sensor response. These synergistic features significantly contribute to the sensor's improved sensor response and selectivity to ammonia at room temperature. In comparison, the other thin films exhibited lower sensing performance due to their larger grain size and densely packed agglomerates, which limited gas diffusion and reduced the availability of grain boundaries for NH_3 adsorption. A rougher surface topology provides a greater number of active sites, thereby enhancing the adsorption of oxygen molecules involved in surface reactions crucial for gas sensing process. In the case of the BVA5 film, the surface roughness was measured to be approximately 1124 nm, which is significantly higher than other sensing layers. This pronounced roughness contributes to the availability of numerous active sites, further promoting gas-solid interactions. Additionally, the incorporation of Ag ions as dopants contributes to improved sensing performance by inducing morphological changes and reducing the crystallite size. XRD analysis confirmed a reduction in crystallite size from around 36.33 nm in the pristine BiVO4 (BVA0) film to approximately 32.99 nm in the 5 wt.% Ag doped BiVO4 (BVA5) thin film sensor. This decrease in crystallite size leads to an increased surface area, enabling more effective contact between gas molecules and the sensing layer [50,51]. Consequently, these structural and morphological features collectively enhance the BVA5 sensor's sensor response at room temperature. XPS analysis revealed an increased concentration of oxygen vacancies in the BVA5 film, which significantly promote interactions towards target gas. These vacancies serve as active sites for oxygen adsorption and facilitate the diffusion of NH_3 gas molecules, thereby contributing to improved gas sensing performance.

It is important to highlight that the incorporation of Ag atoms in the $BiVO_4$ film (BVA5) results in several beneficial modifications, including a smaller crystallite size (32.99 nm), reduced bandgap (2.71 eV), higher surface roughness (1127 nm), abundant nanograin morphology with reduced particle size (60.35 nm), increased oxygen vacancy concentration (32.20 %), and enhanced catalytic activity. For comparison, the overall gas sensing performance of previously reported sensors toward NH_3 gas is summarized in Table 3, further confirming the superior characteristics of the BVA5 film. These combined factors significantly promote NH_3 gas diffusion and charge transfer processes, thereby improving the overall sensing performance of the BVA5 film and making it highly suitable for room-temperature ammonia detection.

2.7. Post-mortem studies of BVA5 films

The interaction between the BVA5 sensing layer and the target gas (NH_3) at room temperature was investigated using X-ray photoelectron spectroscopy (XPS). The results revealed distinct changes only on elemental composition and especially in surface-adsorbed oxygen

Table 3
Comparison of NH_3 gas sensing performance between the present study and previously reported literature.

Material	Synthesis Method	Sensor response (S)	Gas Concentration (ppm)	Operating Temperature (°C)	Discussion	References
$CrVO_4$ nanoparticles	Co-precipitation	32 %	10 ppm	330 °C	The sensing mechanism is primarily a surface band bending phenomenon caused by the adsorption and desorption of ammonia on the material's rough surface, which is created by aggregated nanoparticles.	[52]
Layered Bi_2Se_3/Bi_2O_3 heterostructure	Hydrothermal synthesis	8.5	180	RT	The physisorption of NH_3 on the Bi_2Se_3 surface leads to charge transfer, which modulates the potential barrier at the p-n junction, changing the current and enhancing the sensor's performance.	[53]
Au-decorated V_2O_5	Thermal decomposition + sputtering	109 %	5 ppm	RT	Excellent response at low concentration; noble metal decoration enhances the catalytic activity and charge transfer, which makes it suitable for exhaled breath analysis.	[54]
V_2O_5 Free-standing nanosheets	RF sputtering	1.2	5 ppm	RT	Modest response, but flexible and scalable fabrication method; important for wearable and portable sensors.	[55]
Bi_2O_3-GO nanocomposite	Microwave-assisted combustion	81.23	50 ppm	RT	Graphene oxide improves adsorption and electron mobility, enhancing detection at room temperature.	[56]
$Bi_2MoO_6/g\text{-}C_3N_4$ heterojunction	Hydrothermal synthesis	13.6	10 ppm	RT	Heterostructure with enhanced oxygen vacancies improves selectivity and efficiency for NH_3 sensing at room temperature.	[57]
Porous V_2O_5/PLLA nanosheets	RF sputtering + R2R imprinting	17	75 ppm	RT	The sensing layer exhibited a threefold higher NH_3 response (~17 at 75 ppm) with faster dynamics, attributed to increased surface area from nanoimprint patterning, highlighting its promise for wearable sensors.	[58]
Ag decorated β-$AgVO_3$ nanorods	Hydrothermal synthesis	25.4 %	1 ppm	RT	Good response at very low concentration (1 ppm); Ag decoration enhances catalytic properties and sensitivity.	[59]
NiO: $BiVO_4$ Nanocomposite	Hydrothermal synthesis	97 %	136	RT	The p-n heterojunction formed by p-type NiO and n-type $BiVO_4$ creates a depletion layer that modulates electrical resistance. As a reducing gas, ammonia (NH_3) donates electrons to this interface, altering the sensor's electrical properties and resulting in a measurable response.	[60]
Porous structure and oxygen vacancy engineered $BiVO_4$	Hydrothermal synthesis	1421	270	RT	The enhanced sensing performance is due to porosity and oxygen vacancies. The porous structure increases the surface area for rapid diffusion of NH_3 molecules. Oxygen vacancies provide active sites, improving NH_3 adsorption and boosting the sensor's response.	[61]
Tetragonal scheelite $BiVO_4$ thin film	Spray pyrolysis	58.20	25	RT	A unique interconnected fibrous thin film morphology tuning yields ultrahigh response with excellent repeatability and durability.	[35]
5 wt.% Ag doped $BiVO_4$ thin film	Spray pyrolysis	159	1 ppm	RT	Noble metal doping introduces defects and enhances catalytic activity, leading to an improved sensor response to NH_3 gas with good repeatability and stability at room temperature.	This work

species, as shown in Fig. 12 (a–d). After NH_3 exposure, the XPS spectra of BVA5 exhibited Bi 4f, V 2p, Ag 3d, and O 1 s peaks, along with the emergence of a nitrogen (N 1 s) signal [62,63]. A weak peak at 400.10 eV in the N 1 s spectrum (Fig. 12(b)) corresponds to nitrogen-containing species formed via redox interactions between the BVA5 surface and N–H functional groups in NH_3 gas. This suggests chemisorption and partial surface oxidation of NH_3 molecules rather than complete catalytic conversion into nitrogenous products (i.e., N_2, NO_x) at RT. Furthermore, the surface-adsorbed oxygen component in the O 1 s spectrum significantly decreased from 32 % to 17.22 %, indicating active involvement of these oxygen species in the redox process (Fig. 12 (d)) [63,64]. However, no XPS evidence of additional nitrogen-containing byproducts (e.g., NO_x or N_2) was observed, implying adsorptive interaction with minor surface redox activity, but not catalytic decomposition of NH_3 at room temperature [62–64]. These findings confirm strong surface adsorption and partial redox reaction between NH_3 and the BVA5 sensing film, which aligns well with the observed sensor performance and long-term stability.

3. Conclusion

In summary, pristine and Ag-doped $BiVO_4$ thin films were successfully deposited using a custom-built spray pyrolysis setup. The films were comprehensively analyzed for their structural, optical, morphological, and elemental characteristics to confirm phase formation and key physicochemical properties. The gas sensing performance of the films was then evaluated against various volatile organic compounds. Among them, the 5 wt.% Ag-doped $BiVO_4$ film (BVA5) demonstrated the highest sensor response (S = Igas/Iair = 159), along with a good response time (249 s) and fast recovery time (17 s) for 1 ppm of NH_3 at room temperature. This enhanced performance is attributed to the synergistic effects of a higher dislocation network, narrower bandgap, increased surface roughness, and abundant oxygen vacancies, which together facilitate efficient gas adsorption and diffusion. The sensor also exhibited excellent repeatability and stable performance over a prolonged period (70 days). These results indicate that the BVA5 film is a promising candidate for reliable ammonia detection at room temperature.

Author statement

A declaration that the manuscript is original, has not been published elsewhere, and is not under consideration for publication elsewhere.

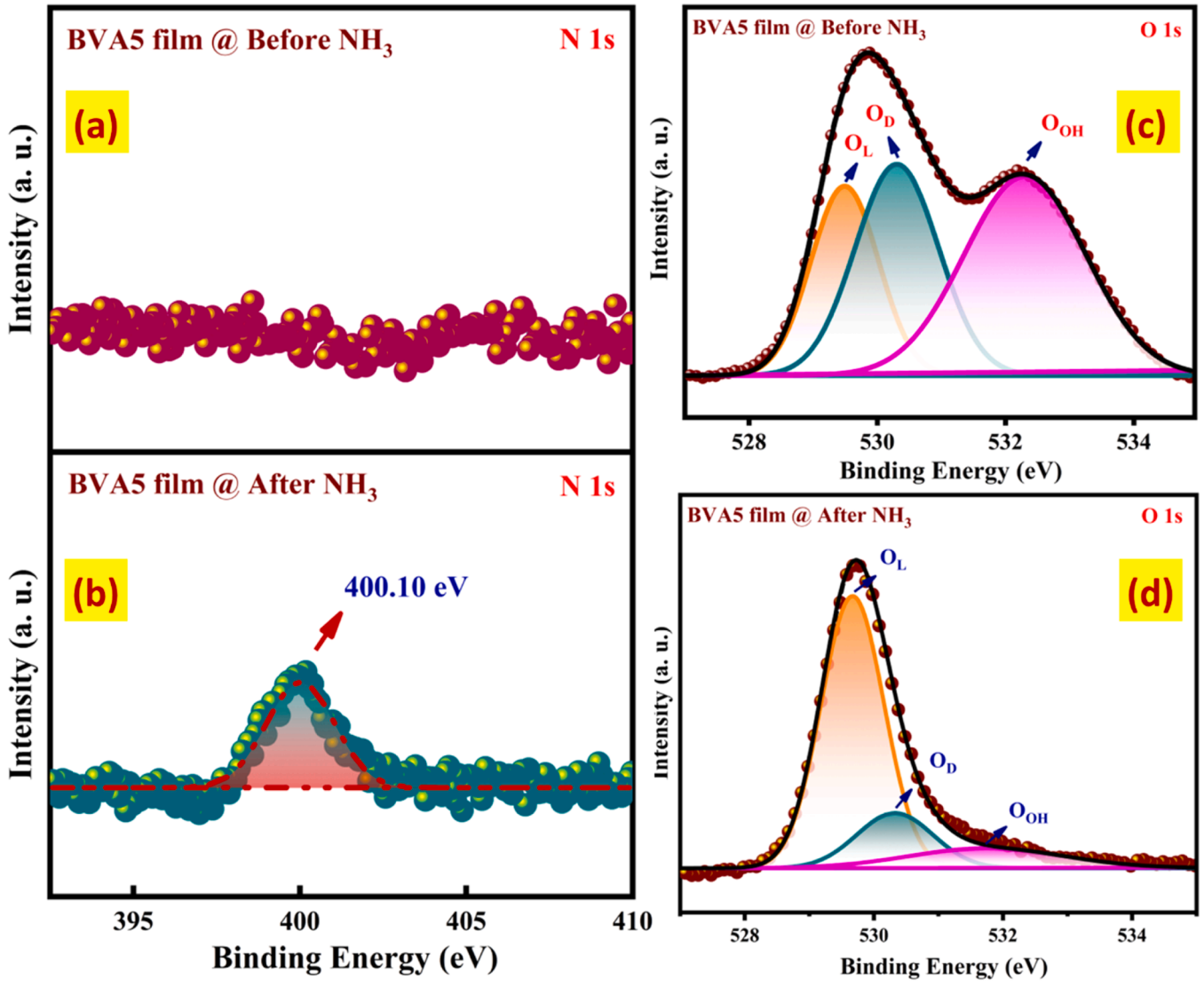

Fig. 12. Shows high-resolution XPS spectra of the BVA5 film studied before and after exposure to NH_3 gas at room temperature: (a-b) N 1 s region and (c-d) O 1 s region.

CRediT authorship contribution statement

Santhosh Nallakumar: Writing – review & editing, Writing – original draft, Visualization, Validation, Software, Methodology, Investigation, Formal analysis, Data curation, Conceptualization. **Logu Thirumalaisamy:** Writing – review & editing, Methodology, Formal analysis. **Kalainathan Sivaperuman:** Writing – review & editing, Investigation, Formal analysis. **Thangavel Ravikumar:** Writing – review & editing, Methodology, Formal analysis, Conceptualization. **Anju Thomas:** Writing – review & editing, Formal analysis, Conceptualization. **Vijaya B:** Writing – review & editing, Methodology, Formal analysis, Conceptualization. **Anand Sekar:** Writing – review & editing, Methodology, Formal analysis, Conceptualization. **Uma Mageshwari P:** Writing – review & editing, Formal analysis. **Manohar Darla:** Writing – review & editing, Formal analysis, Conceptualization. **Ravi Shanker Babu:** Writing – review & editing, Investigation, Formal analysis, Conceptualization. **Usha Rani Muthurakku:** Writing – review & editing, Supervision, Project administration, Conceptualization.

Declaration of competing interest

The authors declare that they have no known competing financial interests or personal relationships that could have appeared to influence the work reported in this paper.

Acknowledgements

The authors would like to acknowledge VIT management for the facilities provided for this work. The authors also would like to convey their gratefulness to all the lab members.

Supplementary materials

Supplementary material associated with this article can be found, in the online version, at doi:10.1016/j.surfin.2025.108306.

Data availability

Data will be made available on request.

References

[1] B.M. Oh, N.Y. Cho, E.H. Lee, S.Y. Park, H.J. Eun, J.H. Kim, Colorimetric and fluorometric bimodal amine chemosensor based on deprotonation-induced intramolecular charge transfer: application to food spoilage detection, J. Hazard. Mater. 465 (2024), https://doi.org/10.1016/j.jhazmat.2023.133150.
[2] M. Hjiri, S. Algessair, R. Dhahri, H.B. Albargi, N. Ben Mansour, A.A. Assadi, G. Neri, Ammonia gas sensors based on undoped and Ca-doped ZnO nanoparticles, RSC Adv. 14 (2024) 5001–5011, https://doi.org/10.1039/d3ra08181h.
[3] R. Pandeeswari, B.G. Jeyaprakash, P. Veluswamy, D. Balamurugan, Enhanced selective ammonia detection of spray deposited Cd-doped β-Ga_2O_3 thin films with low hysteresis effect, Ceram. Int. 48 (2022) 29067–29080, https://doi.org/10.1016/j.ceramint.2022.04.303.
[4] S. Tajik, M.B. Askari, S.A. Ahmadi, F.G. Nejad, Z. Dourandish, R. Razavi, H. Beitollahi, A. Di Bartolomeo, Electrochemical sensor based on $ZnFe_2O_4$/RGO nanocomposite for ultrasensitive detection of hydrazine in real samples, Nanomaterials 12 (2022), https://doi.org/10.3390/nano12030491.
[5] A. Dey, Semiconductor metal oxide gas sensors: a review, Mater. Sci. Eng.: B 229 (2018) 206–217, https://doi.org/10.1016/j.mseb.2017.12.036.
[6] S. Li, W. Wu, X. Yan, Structural and performance regulation of binary transition-metal oxides toward supercapacitors: advances and prospects, Renewables 1 (2023) 142–168, https://doi.org/10.31635/renewables.023.202200010.
[7] D. Meena, M. Jain, M.C. Bhatnagar, Resistive gas sensors based on nanostructured ternary metal oxide: a review, J. Mater. Sci. 59 (2024) 12177–12218, https://doi.org/10.1007/s10853-024-09903-y.
[8] S. Karmakar, A. Sett, P.C. Maity, G. Karmakar, R. Sha, T.K. Bhattacharyya, I. Lahiri, A room-temperature gas sensor based on 2D Ni-Co-Zn ternary oxide nanoflakes for selective and sensitive ammonia detection, Dalton Trans. 52 (2023) 16500–16512, https://doi.org/10.1039/d3dt02751a.
[9] Y. Li, X. Xiao, Z. Ye, Facile fabrication of tetragonal scheelite (t-s) $BiVO_4$/g-C_3N_4 composites with enhanced photocatalytic performance, Ceram. Int. 44 (2018) 7067–7076, https://doi.org/10.1016/j.ceramint.2018.01.143.
[10] L. Thirumalaisamy, Z. Wei, K.R. Davies, M.G. Allan, J. McGettrick, T. Watson, M. F. Kuehnel, S. Pitchaimuthu, Dual shield: bifurcated coating analysis of multilayered WO_3/$BiVO_4$/TiO_2/NiOOH photoanodes for sustainable solar-to-hydrogen generation from challenging waters, ACS Sustain. Chem. Eng. 12 (2024) 3044–3060, https://doi.org/10.1021/acssuschemeng.3c06528.
[11] J. Huang, G. Tan, L. Zhang, H. Ren, A. Xia, C. Zhao, Enhanced photocatalytic activity of tetragonal $BiVO_4$: influenced by rare earth ion Yb^{3+}, Mater. Lett. 133 (2014) 20–23, https://doi.org/10.1016/j.matlet.2014.06.123.
[12] G.S. Natarajamani, V.P. Kannan, S. Madanagurusamy, S. Madanagurusamy, Unveiling LiF-engineered MXene: a novel $Ti_3C_2T_x$/ZnO hybrid composite for highly selective and sensitive chemiresistive NH_3 detection via Schottky barrier modulation at ambient temperature, J. Mater. Chem. A Mater (2025), https://doi.org/10.1039/d5ta01880c.
[13] C. Li, X. Qiao, J. Jian, F. Feng, H. Wang, L. Jia, Ordered porous $BiVO_4$ based gas sensors with high selectivity and fast-response towards H_2S, Chem. Eng. J. 375 (2019), https://doi.org/10.1016/j.cej.2019.121924.
[14] S. Nallakumar, U.R. Muthurakku, Chemically sprayed pristine and Cd $^{2+}$ incorporated Co_2SnO_4 thin films for low ppm level enhanced chemi - resistive behaviour towards dimethylamine detection at room temperature, J. Hazard. Mater. 469 (2024), https://doi.org/10.1016/j.jhazmat.2024.134041.
[15] P. Geng, L. Wang, M. Du, Y. Bai, W. Li, Y. Liu, S. Chen, P. Braunstein, Q. Xu, H. Pang, MIL-96-Al for Li–S batteries: shape or size? Adv. Mater. 34 (2022) https://doi.org/10.1002/adma.202107836.
[16] S.A.J. Jassim, A.A.R.A. Zumaila, G.A.A. Al Waly, Influence of substrate temperature on the structural, optical and electrical properties of CdS thin films deposited by thermal evaporation, Results Phys. 3 (2013) 173–178, https://doi.org/10.1016/j.rinp.2013.08.003.
[17] J. Yu, A. Kudo, Effects of structural variation on the photocatalytic performance of hydrothermally synthesized $BiVO_4$, Adv. Funct. Mater. 16 (2006) 2163–2169, https://doi.org/10.1002/adfm.200500799.
[18] M. Kumar, I. Kebaili, R. Vaish, J. El Ghoul, M.U. Khandaker, Ball mill-induced piezocatalysis assessment for dye degradation using $BiVO_4$, Mater. Today Commun. 37 (2023), https://doi.org/10.1016/j.mtcomm.2023.107306.
[19] N. Kannan, P.S. Venkatesh, M.G. Babu, G. Paulraj, K. Jeganathan, Hydrothermally synthesized rGO-$BiVO_4$ nanocomposites for photocatalytic degradation of RhB, Chem. Phys. Impact 6 (2023), https://doi.org/10.1016/j.chphi.2023.100230.
[20] A. Zhang, J. Zhang, Characterization of visible-light-driven $BiVO_4$ photocatalysts synthesized via a surfactant-assisted hydrothermal method, Spectrochim. Acta A Mol. Biomol. Spectrosc. 73 (2009) 336–341, https://doi.org/10.1016/j.saa.2009.02.028.
[21] E. Nurfani, A. Lailani, W.A.P. Kesuma, M.S. Anrokhi, G.T.M. Kadja, M. Rozana, UV sensitivity enhancement in Fe-doped ZnO films grown by ultrafast spray pyrolysis, Opt. Mater. 112 (2021), https://doi.org/10.1016/j.optmat.2020.110768.
[22] I. Loyola Poul Raj, S. Valanarasu, R.S. Rimal Isaac, M. Ramudu, Y. Bitla, V. Ganesh, I.S. Yahia, The role of silver doping in tuning the optical absorption, energy gap, photoluminescence properties of NiO thin films for UV photosensor applications, Optik 254 (2022), https://doi.org/10.1016/j.ijleo.2022.168634.
[23] M. Karyaoui, A. Mhamdi, H. Kaouach, A. Labidi, A. Boukhachem, K. Boubaker, M. Amlouk, R. Chtourou, Some physical investigations on silver-doped ZnO sprayed thin films, Mater. Sci. Semicond. Process. 30 (2015) 255–262, https://doi.org/10.1016/j.mssp.2014.09.017.
[24] D. Alagarasan, S.S. Hegde, R. Naik, H.D. Shetty, H.B.S. Prasad, T. Alshahrani, S. AlFaify, M. Shkir, Remarkable NH_3 gas sensing performance of spray deposited Tb doped WO_3 thin films at room temperature, J. Photochem. Photobiol. A Chem. 459 (2025), https://doi.org/10.1016/j.jphotochem.2024.116087.
[25] S. Kumar, S. Ahirwar, A.K. Satpati, Insight into the PEC and interfacial charge transfer kinetics at the Mo doped $BiVO_4$ photoanodes, RSC Adv. 9 (2019) 41368–41382, https://doi.org/10.1039/c9ra08743e.
[26] B. Zhou, X. Zhao, H. Liu, J. Qu, C.P. Huang, Synthesis of visible-light sensitive M-$BiVO_4$ (M = Ag, Co, and Ni) for the photocatalytic degradation of organic pollutants, Sep. Purif. Technol. 77 (2011) 275–282, https://doi.org/10.1016/j.seppur.2010.12.017.
[27] C. Regmi, D. Dhakal, S.W. Lee, Visible-light-induced Ag/$BiVO_4$ semiconductor with enhanced photocatalytic and antibacterial performance, Nanotechnology 29 (2018), https://doi.org/10.1088/1361-6528/aaa052.
[28] V. Kumar, N. Singh, R.M. Mehra, A. Kapoor, L.P. Purohit, H.C. Swart, Role of film thickness on the properties of ZnO thin films grown by sol-gel method, Thin Solid Films 539 (2013) 161–165, https://doi.org/10.1016/j.tsf.2013.05.088.
[29] A.A. Mane, S.A. Nikam, A.V. Moholkar, NO_2 gas sensing properties of sprayed composite porous MoO_3-V_2O_5 thin films, Mater. Chem. Phys. 216 (2018) 294–304, https://doi.org/10.1016/j.matchemphys.2018.05.043.
[30] D.N.G. Krishna, J. Philip, Review on surface-characterization applications of X-ray photoelectron spectroscopy (XPS): recent developments and challenges, Appl. Surf. Sci. Adv. 12 (2022), https://doi.org/10.1016/j.apsadv.2022.100332.
[31] J.M. Ribeiro, F.C. Correia, P.B. Salvador, L. Rebouta, L.C. Alves, E. Alves, N. P. Barradas, A. Mendes, C.J. Tavares, Compositional analysis by RBS, XPS and EDX of ZnO:Al, Bi and ZnO:Ga, Bi thin films deposited by d.c. magnetron sputtering, Vacuum 161 (2019) 268–275, https://doi.org/10.1016/j.vacuum.2018.12.038.
[32] S. K, J. Peediyekkal, S. M, S. S, M. Chennabasappa, Rietveld refinement, core level electron shell structure and frequency-dependent dielectric behavior of vanadium bismuth oxide microstructures, Phys. B Condens. Matter 691 (2024), https://doi.org/10.1016/j.physb.2024.416318.
[33] S. Singh, R.K. Sahoo, N.M. Shinde, J.M. Yun, R.S. Mane, W. Chung, K.H. Kim, Asymmetric faradaic assembly of Bi_2O_3 and MnO_2 for a high-performance hybrid electrochemical energy storage device, RSC Adv. 9 (2019) 32154–32164, https://doi.org/10.1039/c9ra06331e.

[34] L. Antony, E. Pavitra, K.S. Ranjith, G.S.R. Raju, Y.S. Huh, Y.K. Han, Ag nanoparticles-decorated bimetal complex selenide 3D flowers: a solar energy-driven flexible hybrid supercapacitor for smart wearables, Adv. Fiber Mater. 6 (2024) 529–542, https://doi.org/10.1007/s42765-023-00363-8.
[35] S. Nallakumar, L. Thirumalaisamy, S. Kalainathan, B. Vijaya, A. Sekar, M.U. Rani, Unveiling a growth temperature-dependent ultra-sensitive tetragonal scheelite $BiVO_4$ thin film-based gas sensor for ammonia volatilization at room temperature, RSC Adv. 14 (2024) 39498–39510, https://doi.org/10.1039/d4ra08169b.
[36] F. Liu, Z. Jiang, J. Zhao, C. Chen, H. Zhou, N. Xiang, J. Liu, L. Wu, Creating oxygen vacancies on porous tungsten oxide nanospheres via one-step muffle calcination for ultra-fast detection of ppb-level hydrogen sulfide sensors, J. Alloys Compd. 971 (2024), https://doi.org/10.1016/j.jallcom.2023.172782.
[37] R. Barathy T, P.V.K. Yadav, A. Mondal, B. Ajitha, J. Jarugala, Y.A. Kumar Reddy, High porosity and oxygen vacancy enriched WO_{3-x} thin films for room temperature hydrogen gas sensors, Int. J. Hydrogen Energy 50 (2024) 878–888, https://doi.org/10.1016/j.ijhydene.2023.07.218.
[38] X. Liu, T. Ma, N. Pinna, J. Zhang, Two-dimensional nanostructured materials for gas sensing, Adv. Funct. Mater. 27 (2017), https://doi.org/10.1002/adfm.201702168.
[39] N. Goel, K. Kunal, A. Kushwaha, M. Kumar, Metal oxide semiconductors for gas sensing, Eng. Rep. 5 (2023), https://doi.org/10.1002/eng2.12604.
[40] V. Mounasamy, G.K. Mani, D. Ponnusamy, K. Tsuchiya, A.K. Prasad, S. Madanagurusamy, Template-free synthesis of vanadium sesquioxide (V_2O_3) nanosheets and their room-temperature sensing performance, J. Mater. Chem. A Mater 6 (2018) 6402–6413, https://doi.org/10.1039/c7ta10159g.
[41] C. Fan, J. Yang, W. Ni, J. Wu, X. Liu, Z. Li, Y. Zhang, W. Quan, M. Zeng, N. Hu, H. Fang, T. Wang, Z. Yang, Real-time and wireless transmission of a nitrogen-doped $Ti_3C_2T_x$ wearable gas sensor for efficient detection of food spoilage and ammonia leakage, ACS Sens. 9 (2024) 4870–4878, https://doi.org/10.1021/acssensors.4c01394.
[42] J. Shruthi, N. Jayababu, M.V. Ramana Reddy, Enhanced gas sensing performance of Ag-doped Y_2O_3-CdO nanocomposite-based ammonia sensor, Ceram. Int. (2024), https://doi.org/10.1016/j.ceramint.2024.12.217.
[43] S. Nallakumar, U.R. Muthurakku, Investigation on the impact of film thickness on spray-deposited Co_2SnO_4 thin films gas sensing performance towards dimethylamine detection at room temperature, Surf. Interf. 51 (2024), https://doi.org/10.1016/j.surfin.2024.104666.
[44] H.Y. Li, C.S. Lee, D.H. Kim, J.H. Lee, Flexible room-temperature NH_3 sensor for ultrasensitive, selective, and humidity-independent gas detection, ACS Appl. Mater. Interfaces 10 (2018) 27858–27867, https://doi.org/10.1021/acsami.8b09169.
[45] M.S. Choi, A. Mirzaei, H.G. Na, S. Kim, D.E. Kim, K.H. Lee, C. Jin, S.W. Choi, Facile and fast decoration of SnO_2 nanowires with Pd embedded SnO_{2-x} nanoparticles for selective NO2 gas sensing, Sens. Actuators B Chem. 340 (2021), https://doi.org/10.1016/j.snb.2021.129984.
[46] T. Ravikumar, L. Thirumalaisamy, A. Thomas, S. Nallakumar, S. Pandiaraj, M. Mr, A.N. Alodhayb, S. Pitchaimuthu, V. Dananjaya, C. Abeykoon, K. Sivaperuman, A. N. Grace, Impact of annealing temperature on the response and sensitivity of spinel $ZnFe_2O_4$ thin film to ammonia gas sensing at room temperature, Mater. Today Chem. 43 (2025), https://doi.org/10.1016/j.mtchem.2025.102515.
[47] S. Nallakumar, L. Thirumalaisamy, S. Madhanagurusamy, S. Kalainathan, M. U. Rani, Inverse and distorted Co_2SnO_4 cubic spinel thin films for dimethylamine detection at room temperature, New J. Chem. 47 (2023) 11110–11122, https://doi.org/10.1039/d3nj01409f.
[48] R. Thangavel, K. Sivaperuman, L. Thirumalaisamy, S. Pandiaraj, M. Alruwaili, N. Alanazi, A.N. Alodhayb, C. Abeykoon, A.N. Grace, Unleashing synergy: rGO decorated on a cobalt-doped $ZnFe_2O_4$ film to detect trace-level NH_3 at ambient temperature with high response and cross-selectivity, ACS Appl. Electron. Mater. (2025), https://doi.org/10.1021/acsaelm.5c00618.
[49] K. Sivaperuman, A. Thomas, R. Thangavel, L. Thirumalaisamy, S. Palanivel, S. Pitchaimuthu, N. Ahsan, Y. Okada, Binary and ternary metal oxide semiconductor thin films for effective gas sensing applications: a comprehensive review and future prospects, Prog. Mater. Sci. 142 (2024), https://doi.org/10.1016/j.pmatsci.2023.101222.
[50] T. Ravikumar, K. Sivaperuman, Branched $ZnFe_2O_4$ nanorods grown via chemical spray pyrolysis technique for chemiresistive xylene gas sensor, Colloids Surf. A Physicochem. Eng. Asp. 686 (2024), https://doi.org/10.1016/j.colsurfa.2024.133382.
[51] B.Y. Song, C. Li, X.F. Zhang, R. Gao, X.L. Cheng, Z.P. Deng, Y.M. Xu, L.H. Huo, S. Gao, A highly sensitive and selective nitric oxide/butanone temperature-dependent sensor based on waste biomass-derived mesoporous SnO_2 hierarchical microtubes, J. Mater. Chem. A Mater 10 (2022) 14411–14422, https://doi.org/10.1039/d2ta03299f.
[52] D.J. Dmonte, A. Bhardwaj, P. Kavraz, R. Slobodian, J. Antos, O. Sisman, D. Galusek, T. Fischer, S. Mathur, I. Kuritka, Detection of NH_3 gas using $CrVO_4$ nanoparticles, Sens. Actuators B Chem. 406 (2024), https://doi.org/10.1016/j.snb.2024.135380.
[53] B. Das, S. Riyajuddin, K. Ghosh, R. Ghosh, Room-temperature ammonia detection using layered Bi_2Se_3/Bi_2O_3: a next-generation sensor, ACS Appl. Electron. Mater. 5 (2023) 948–956, https://doi.org/10.1021/acsaelm.2c01496.
[54] K. Malook, H. Khan, M. Shah, I.U. Haque, A. Ahmad, Fabrication of Au-decorated V_2O_5 based sensor for ultra trace level detection of ammonia in an environment resembling human exhaled breath, J. Alloys Compd. 1010 (2025), https://doi.org/10.1016/j.jallcom.2024.177089.
[55] V. Mounasamy, G.K. Mani, K. Tsuchiya, S. Madanagurusamy, Preparation of free-standing V_2O_5 nanosheets for ammonia sensing application: a potential candidate for flexible sensors, J. Sci.: Adv. Mater. Dev. 7 (2022), https://doi.org/10.1016/j.jsamd.2021.100415.
[56] B.G. Ghule, N.M. Shinde, S.D. Raut, S.F. Shaikh, A.M. Al-Enizi, K.H. Kim, R. S. Mane, Porous metal-graphene oxide nanocomposite sensors with high ammonia detectability, J. Colloid Interface Sci. 589 (2021) 401–410, https://doi.org/10.1016/j.jcis.2020.12.096.
[57] K. Wu, X. Qiu, Y. Luo, C. Zhang, Oxygen vacancy mediated-bismuth molybdate/graphitic carbon nitride type II heterojunction chemiresistor for efficient NH_3 detection at room temperature, ACS Sens. (2024), https://doi.org/10.1021/acssensors.4c02307.
[58] V. Mounasamy, G.K. Mani, K. Tsuchiya, S. Madanagurusamy, Nanoimprint assisted free standing porous vanadium oxide nanosheet based ammonia sensor, Appl. Surf. Sci. 541 (2021), https://doi.org/10.1016/j.apsusc.2020.148271.
[59] P.G. Su, J.J. Yang, Preparation and NH_3 gas-sensing properties of Ag/β-$AgVO_3$ nanorods, Anal. Methods 16 (2024) 3058–3066, https://doi.org/10.1039/d4ay00255e.
[60] H. Seema, S. Zaman, M. Zahid, Z. Zafar, T. Akitsu, Facile preparation and green synthesis of Ni/$BiVO_4$ sensor for room temperature NH_3 sensing, J. Indian Chem. Soc. 102 (2025), https://doi.org/10.1016/j.jics.2025.101700.
[61] R. Paul, N. Maity, B. Das, S. Rani, K. Ghosh, S. Lisenkov, I. Ponomareva, R. Ghosh, Controllable oxygen vacancy defect engineering of $BiVO_4$ porous structures for room temperature NH_3 detection, Chem. Eng. J. 515 (2025), https://doi.org/10.1016/j.cej.2025.163814.
[62] T.V. Beatriceveena, E. Prabhu, A. Sree Rama Murthy, V. Jayaraman, K. I. Gnanasekar, Highly selective PbS thin film based ammonia sensor for inert ambient: in-situ hall and photoelectron studies, Appl. Surf. Sci. 456 (2018) 430–436, https://doi.org/10.1016/j.apsusc.2018.06.145.
[63] G.L. Chen, M.S. Lv, L.L. Sui, Z.P. Deng, Y.M. Xu, L.H. Huo, S. Gao, Low-temperature and dual-sensing NO_2/dimethylamine sensor based on single-crystal WO_3 nanoparticles-supported sheets synthesized by simple pyrolysis of spoiled WCl_6 powder, Chem. Eng. J. 464 (2023), https://doi.org/10.1016/j.cej.2023.142528.
[64] X. Sun, R. Gao, Y. Wu, X. Zhang, X. Cheng, S. Gao, Y. Xu, L. Huo, Novel in-situ deposited V_2O_5 nanorods array film sensor with enhanced gas sensing performance to n-butylamine, Chem. Eng. J. 459 (2023), https://doi.org/10.1016/j.cej.2023.141505.